Geophys. J. Int. (2007) **169,** 367–379 doi: 10.1111/j.1365-246X.2006.03310.x

Temporal and spatial variations of post-seismic deformation following the 1999 Chi-Chi, Taiwan earthquake

Ya-Ju Hsu,[1,2] Paul Segall,[3] Shui-Beih Yu,[1] Long-Chen Kuo[1] and Charles A. Williams[4]

[1] *Institute of Earth Sciences, Academia Sinica, Nankang, Taipei, Taiwan. E-mail: yaru@earth.sinica.edu.tw*
[2] *Division of Geological and Planetary Sciences, California Institute of Technology, Pasadena,* CA 91125*, USA*
[3] *Department of Geophysics, Stanford University, California, USA*
[4] *Department of Earth and Environmental Sciences, Rensselaer Polytechnic Institute, New York, USA*

Accepted 2006 November 2. Received 2006 October 30; in original form 2006 June 16

SUMMARY

We use GPS displacements collected in the 15 months after the 1999 Chi-Chi, Taiwan earthquake (M_w 7.6) to evaluate whether post-seismic deformation is better explained by afterslip or viscoelastic relaxation of the lower crust and upper mantle. We find that all viscoelastic models tested fail to fit the general features in the post-seismic GPS displacements, in contrast to the satisfactory fit obtained with afterslip models. We conclude that afterslip is the dominant mechanism in the 15-month period, and invert for the space–time distribution of afterslip, using the Extended Network Inversion Filter. Our results show high slip rates surrounding the region of greatest coseismic slip. The slip-rate distribution remains roughly stationary over the 15-month period. In contrast to the limited coseismic slip on the décollement, afterslip is prominent there. Maximum afterslip of 0.57 m occurs downdip and to the east of the hypocentral region. Afterslip at hypocentral depths is limited to the southern part of the main shock rupture, with little or no slip on the northern section where coseismic slip was greatest. Whether this results from along strike variations in frictional properties or dynamic conditions that locally favour stable sliding is not clear. In general, afterslip surrounds the area of greatest coseismic slip, consistent with post-seismic slip driven by the main shock stress change. The total accumulated geodetic afterslip moment is 3.8×10^{19} N m, significantly more than the seismic moment released by aftershocks, 6.6×10^{18} N m. Afterslip and aftershocks appear to have different temporal evolutions and some spatial correlations, suggesting that aftershock rates may not be completely controlled by the rate of afterslip.

Key words: afterslip, Chi-Chi earthquake, postseismic deformation, viscoelastic relaxation.

1 INTRODUCTION

The 1999 September 21 Chi-Chi, Taiwan, earthquake (M_w 7.6) caused a 100-km-long surface rupture, mainly following the north–south trending Chelungpu thrust fault (CLPF). The surface rupture turned east–west at the northern end of CLPF where the maximum horizontal and vertical surface displacements of up to 8–10 m were recorded (Lee *et al.* 2002). Coseismic GPS displacements showed NW–NNW directed horizontal movements of 1.1–9.1 m and vertical uplift of 1.2–4.4 m on the hangingwall. In contrast, much smaller SE–SEE directed horizontal movements of 0.1–1.5 m and slight subsidence of 0.02–0.26 m were found on the footwall (Yu *et al.* 2001).

Inversions of geodetic and seismic data for the coseismic slip distribution are in general agreement. All show a maximum slip of about 10–15 m concentrated at the northern end of the fault, and extending about 10 km downdip from the ground surface (Ji *et al.* 2001; Johnson *et al.* 2001; Ma *et al.* 2001; Zeng & Chen 2001; Dominguez *et al.* 2003; Loevenbruck *et al.* 2004). In contrast, the net slip at the southern end of the fault near the hypocentre is only 1–2 m.

The post-seismic GPS displacements, after removing secular motions, show east over west thrusting, similar to the displacement field due to the main shock (Yu *et al.* 2003) (Fig. 1). These authors model the GPS time-series as a combination of a linear trend and an exponential decay with a relaxation time estimated to be 86 days. Hsu *et al.* (2002) and Yu *et al.* (2003) conclude that afterslip is the dominant mechanism of post-seismic deformation following the Chi-Chi earthquake. Perfettini & Avouac (2004) use the data from Yu *et al.* (2003) to suggest that post-seismic displacements result from afterslip governed by steady-state velocity strengthening friction with $a = \partial\mu/\partial \log(V)$, of about $10^{-2} \sim 10^{-3}$, where a is a constitutive parameter, μ is the coefficient of friction and V is the sliding velocity. They also suggest that the rate of aftershock activity is driven by the rate of afterslip.

Another common mechanism invoked to explain post-seismic deformation is viscoelastic relaxation of the lower crust and upper mantle (Nur & Mavko 1974; Pollitz 2001; Sheu & Shieh 2004). Sheu

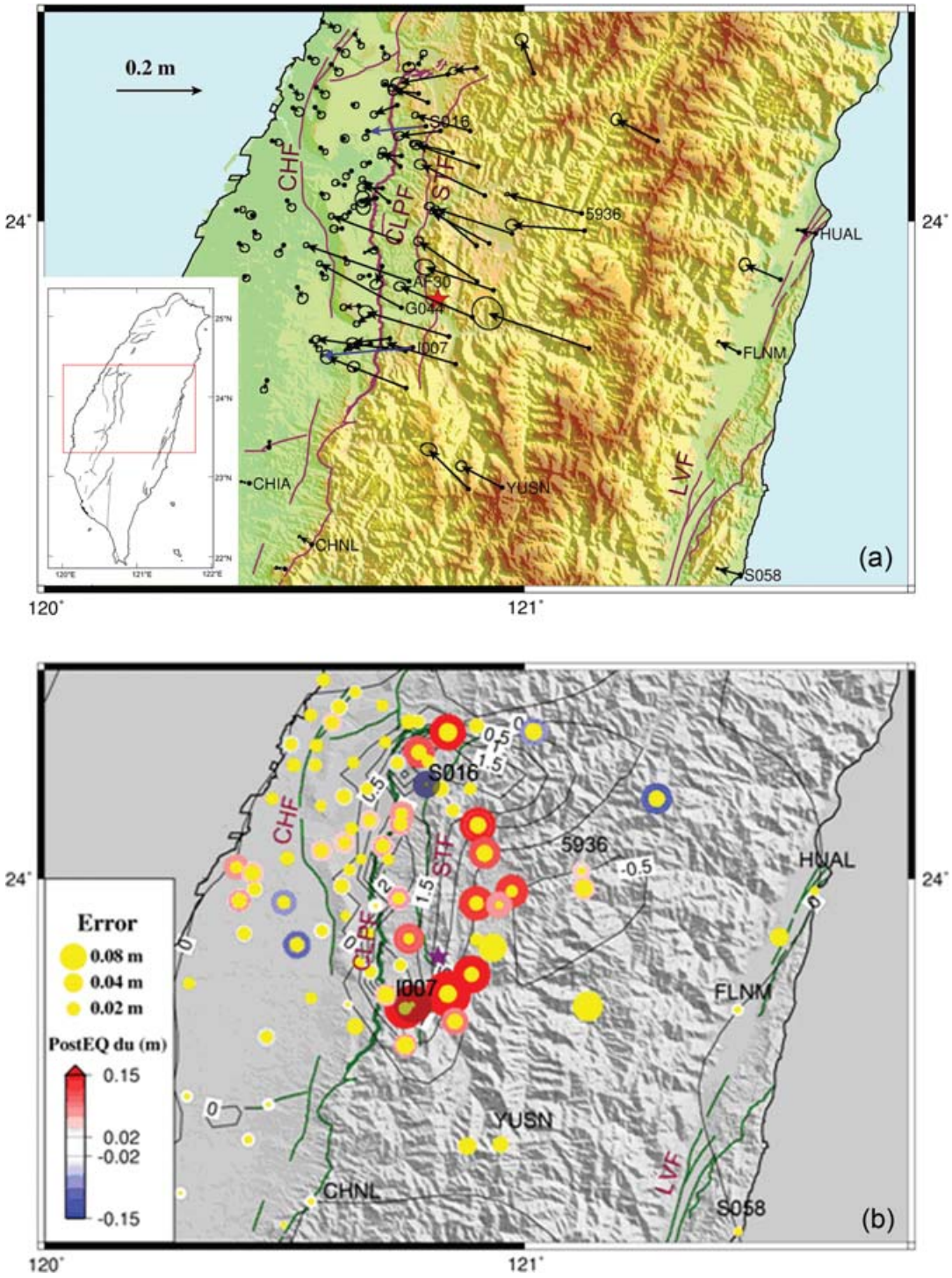

Figure 1. Post-seismic displacements during the 15-month period, 1999 September to 2000 December, after the Chi-Chi earthquake. Method for determining displacements is discussed in text. (a) Horizontal displacements are shown by black vectors with 95 per cent confidence ellipses. Blue vectors show two continuous stations, S016 and I007, not modelled in our study. The red star denotes the epicentre of the main shock. Major faults are indicated as purple lines (1999 Chi-Chi rupture in thicker line). CHF: the Changhua fault, CLPF: the Chelungpu fault, STF: the Shuantung fault, LVF: the Longitudinal Valley Fault. (b) Vertical displacements are shown by circles with uplift and subsidence indicated by red and blue colours, respectively. Dark blue and red circles show two continuous stations that were not modelled in our study. The yellow circles are standard deviations. Black contours on the background indicate coseismic vertical displacement in metres. (Data from Yu *et al.* 2003).

& Shieh (2004) analysed GPS post-seismic displacements in the 97-day period after the Chi-Chi main shock and concluded that afterslip and viscoelastic relaxation dominated post-seismic deformation in the near and far field, respectively.

In this study, we examine two possible mechanisms including viscoelastic relaxation using a 2-D finite element model as well as afterslip using the Extended Network Inversion Filter (Segall & Matthews 1997; McGuire & Segall 2003). We consider these

mechanisms and discuss the implication of the inferred parameters for crust–mantle rheology as well as the frictional properties of the fault zone. Note that we do not consider interaction between viscoelastic relaxation and afterslip, nor do we consider poroelastic relaxation as a possible post-seismic process (Jonsson *et al.* 2003; Fialko 2004). Preliminary modelling did not favour a poroelastic model for the Chi-Chi post-seismic data, so we focus on comparing and contrasting afterslip and viscoelastic relaxation.

2 DATA

We use post-seismic GPS displacements from Yu *et al.* (2003) collected by several agencies, including the Institute of Earth Sciences, Academia Sinica (IESAS), Central Weather Bureau (CWB) and the Land Survey Bureau (LSB), Ministry of Interior. Yu *et al.* (2003) processed the campaign and continuous GPS data using the Bernese v.4.2 software (Hugentobler *et al.* 2001), using precise ephemerides from the International GNSS services (IGS). The International Terrestrial Reference Frame 1997 (ITRF97) was adopted by taking the ITRF97 coordinates and velocities of an IGS core site, TSKB (Tsukuba, Japan) as a reference station. Yu *et al.* (2003) gives a more detailed description of the GPS data acquisition and processing. The GPS displacements from 45 permanent GPS stations and seven campaign surveys of 80 stations conducted between 1999 September and 2000 December well characterize the post-earthquake deformations.

We choose to exclude stations biased by poor sky visibility, unstable monuments, or that have insufficient number of observations. About 60 per cent of the campaign GPS sites were not modelled because they were surveyed less than six times following the earthquake. Two continuous GPS sites near the rupture area, I007 and S016, were also not modelled because their motions are not consistent with the displacements of neighbouring stations (Fig. 1). Station I007 was influenced by a M_w 6.3 aftershock on 1999 September 25; ground cracks were observed near the station subsequent to the aftershock and the monument had tilted. In summary, we analyse data from seven continuous stations and 25 campaign stations that were surveyed at least six times in the 15 months after the earthquake. In order to isolate post-earthquake transients, we subtract estimated secular motions from the time-series at each station prior to inversion. The secular velocities for some stations installed after the main shock are interpolated from pre-existing stations with repeated GPS data between 1992 and 1999 in central Taiwan (Yu *et al.* 2001). Uncertainties in the secular correction are propagated into the data covariance matrices in the time-dependent inversion described in Section 4.

The post-earthquake GPS displacements include both aseismic deformation and displacements due to large aftershocks (Fig. 2). Chi & Dreger (2004) suggest that a large portion of the post-seismic deformation may be attributed to aftershocks. However, most of the GPS stations were installed after the occurrence of the largest aftershocks. In addition, we isolate aseismic deformation by estimating offsets in the GPS time-series at the time of four major aftershocks ($M_w > 6$). We infer that the influence of remaining aftershocks on the post-seismic measurements is small.

3 VISCOELASTIC RELAXATION

We calculate viscoelastic displacements in a 2-D model using the finite element package LithoMop (http://www.geodynamics.org:8080/cig/software/packages/lithomop/), that has been modified from the code TECTON (Melosh & Raefsky 1980; Williams & Richardson 1991) using the Pyre http://www.cacr.caltech.edu/projects/pyre computational framework. We checked the program by comparing results with analytical solutions for homogemeous elastic and viscoelatic half-spaces. The 2-D model grid used here extends horizontally 800 km from the CLPF on both sides. The vertical domain extends to 1200 km depth. An enlargement of the model region is shown in Fig. 3. The grid spacing near the fault is less than 1 km and varies laterally and vertically, crudely corresponding to the expected strain gradient. We use a simplified coseismic fault geometry and slip distribution of the Chi-Chi earthquake based on previous results (Yu *et al.* 2003; Johnson & Segall 2004). The averaged coseismic slip of 4 and 1 m, taken from the 3-D coseismic slip inversions, are assigned to the main rupture plane and the lower décollement, respectively.

We assume that crust and mantle can be described by a Newtonian Maxwell viscoelastic rheology and calculate surface displacements over the 15-month period after the main shock. A displacement-fixed boundary condition is specified on the side-walls and the bottom wall. Two models with different rheological structures are presented here (Fig. 3). For the model in Fig. 3(a), there are no lateral variations in viscosity. The model consists of three layers including an elastic upper crust at 0–20 km depth, a viscoelastic lower crust with viscosity 10^{18} Pa s from 20 to 40 km depth, and a viscoelastic upper mantle with viscosity 10^{20} Pa s at depths greater than 40 km. The Moho discontinuity at 40 km depth is roughly consistent with a tomographic model from simultaneous inversion of local earthquake *P*-wave arrival times and *P*-wave velocity structures (Rau & Wu 1995). We choose a low viscosity in the lower crust to investigate whether viscoelastic deformation alone can explain the post-seismic deformation.

The GPS displacements are taken from the region of maximum displacement, between 23.7°N and 24.0°N and projected onto a profile perpendicular to the fault (Fig. 4). We find that the predicted viscoelastic displacement vectors are opposite in direction to the GPS displacements near the fault (Fig. 4a). In particular, the observed horizontal displacements within 10 km on the hangingwall are directed down to the west, whereas the predicted displacements are up to the east. In contrast, an afterslip model, taken from the results of Yu *et al.* (2003), fits the data reasonably well. For models including a combination of viscoelastic relaxation and afterslip, the viscoelastic model only improves the fit at distant (more than 40 km) GPS stations on the hangingwall. In addition, the viscoelastic model predicts displacements on the footwall that significantly exceed the observed displacements.

We find that these general features do not vary significantly with more realistic fault geometry and coseismic slip distributions. The induced deformation estimated from different models of coseismic slip distributions show similar features. Altering the viscosity structure produces patterns of displacement similar to those seen in Fig. 4(a). In particular, increasing the viscosity of the crustal layer by a factor of 10 causes the maximum displacements to decrease by a factor of 10, but otherwise leaves the spatial pattern unchanged. Changing the viscosity of upper mantle by a factor of 10 causes little variation of maximum displacement (less than 10 per cent).

For the model shown in Fig. 3(b), we add a low viscosity block that corresponds to the region with high heat flow and absence of seismicity before and after Ch-Chi earthquake beneath the Central Range (Fig. 2) (Lin 2000; Ma *et al.* 2005). The model displacements show similar directions to the GPS displacements on the hangingwall, although the amplitude is much too small to explain the surface displacements by viscoelastic flow alone (Fig. 4b). We can increase the amplitude of the displacements on the hangingwall by reducing

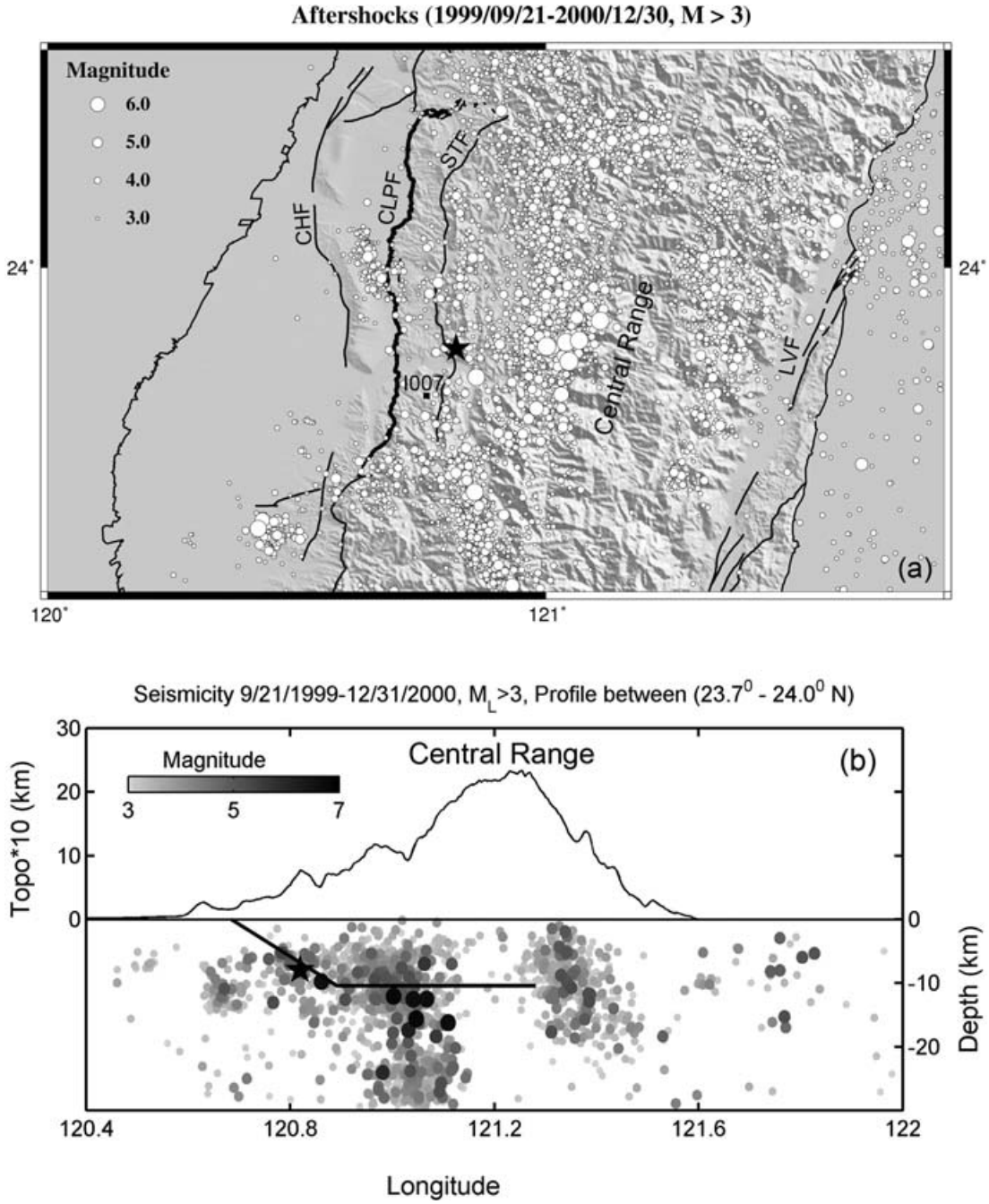

Figure 2. Aftershocks in the 15-month period, 1999 September to 2000 December, with magnitude greater than 3. (a) The circles denote aftershock and their sizes are proportional to magnitude. Major faults are indicated as solid lines (1999 Chi-Chi rupture in thicker line). Continuous GPS station I007 is identified by solid square. (b) A aftershock profile between 23.7° N and 24.0° N. Black solid lines at depth show the model fault geometry. Data from the Central Weather Bureau, Taiwan.

the viscosity of lower crust. However, the model displacements on the footwall also increase in amplitude, contradicting the GPS observations.

Although our model is 2-D, we expect that the displacement patterns for 2-D and 3-D viscoelastic models are similar. The exception is that the displacements decay more rapidly with distance from the fault in three dimensions. The comparison between the viscoelastic and afterslip models is biased by the fact that the afterslip models are inversions whereas the viscoelastic calculations are forward models. Nevertheless, forward calculations over a range of viscosities, given the two classes of rheological structures shown in Fig. 3, have not yielded a viscoelastic model that fits the general features in the GPS displacements. This implies the post-seismic deformation mainly results from afterslip. Nevertheless, it is possible that viscoelastic relaxation contributes to deformation in the far-field, particularly on the east coast of Taiwan.

4 SPACE–TIME DEPENDENT INVERSION OF AFTERSLIP

In the following calculations we assume all surface deformation is due to slip on the fault and employ the Network Inversion Filter, NIF

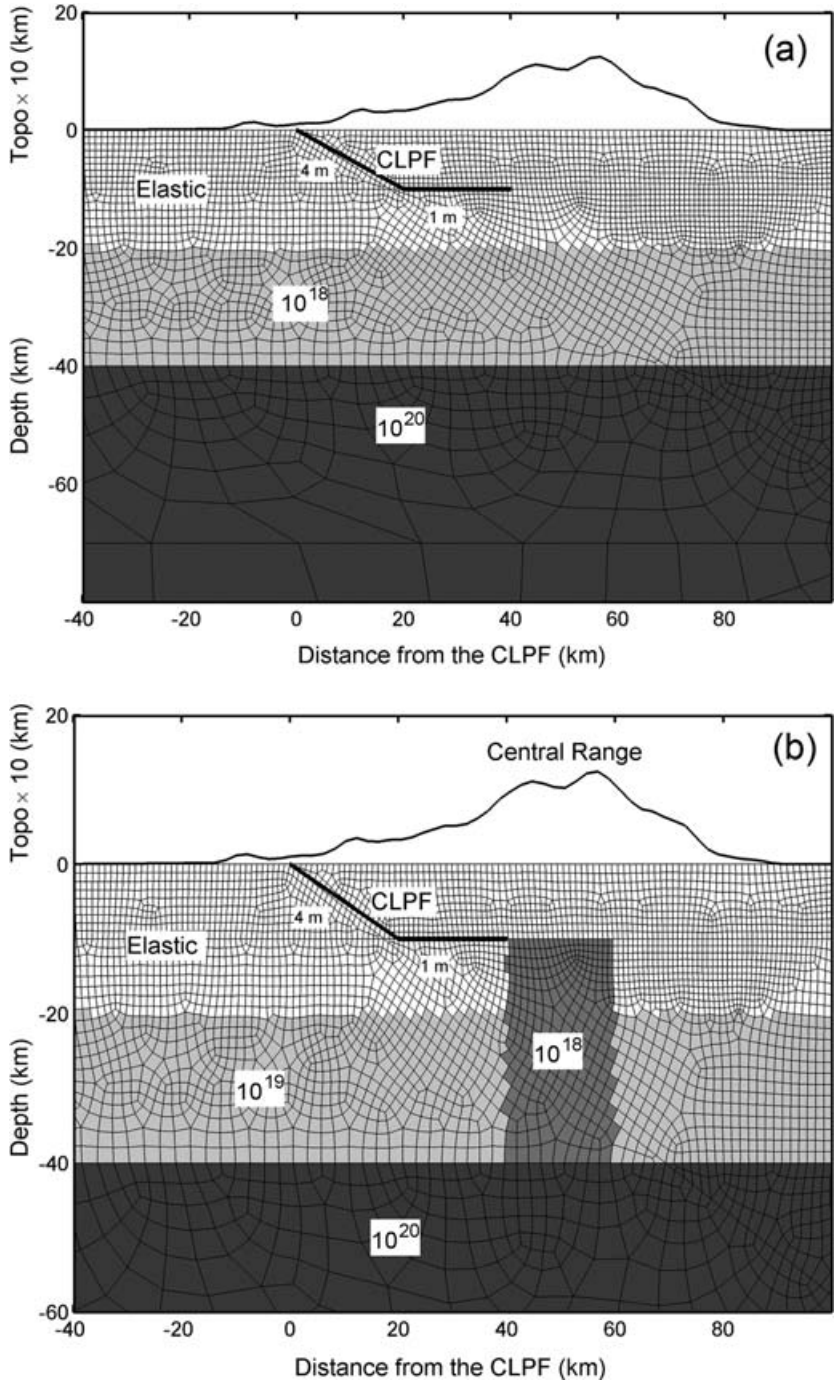

Figure 3. The mesh configuration for the finite element computations. (a) A viscoelastic model consisting of upper crust, lower crust and upper mantle. The black solid line and values indicate the position of fault and coseismic slip on it, respectively. The number in each layer denotes viscosity. (b) A model consisting of three layers and a low viscosity block beneath the Central Range.

(Segall & Matthews 1997), to invert for the evolution of afterslip with space and time. This approach is based on a Kalman filter and is capable of extracting spatially coherent signals, such as transient fault slip, from incoherent signals, such as local benchmark motions. Rather than assuming logarithmic or exponential functions of time (Hsu *et al.* 2002; Yu *et al.* 2003), the NIF allows non-parametric estimation by employing a stochastic model for the temporal evolution of fault slip. The NIF has been applied to several different data sets, including post-seismic deformation following the Loma Prieta and Izmit earthquakes (Segall *et al.* 2000; Burgmann *et al.* 2002), as well as aseismic slip transients in Cascadia (McGuire & Segall 2003) and Japan (Miyazaki *et al.* 2004, 2006). McGuire & Segall (2003) incorporate non-negativity constraints on fault slip rate as well as direct estimation of the system hyperparameters, which determine the appropriate amount of spatial and temporal smoothing. The approach employs an extended Kalman filter and is, therefore, referred to as an Extended Network Inversion Filter (ENIF).

The NIF was originally designed to detect subtle transients, from background deformation that is steady in time. The stochastic model assumed that the slip accelerations are small and random. This leads

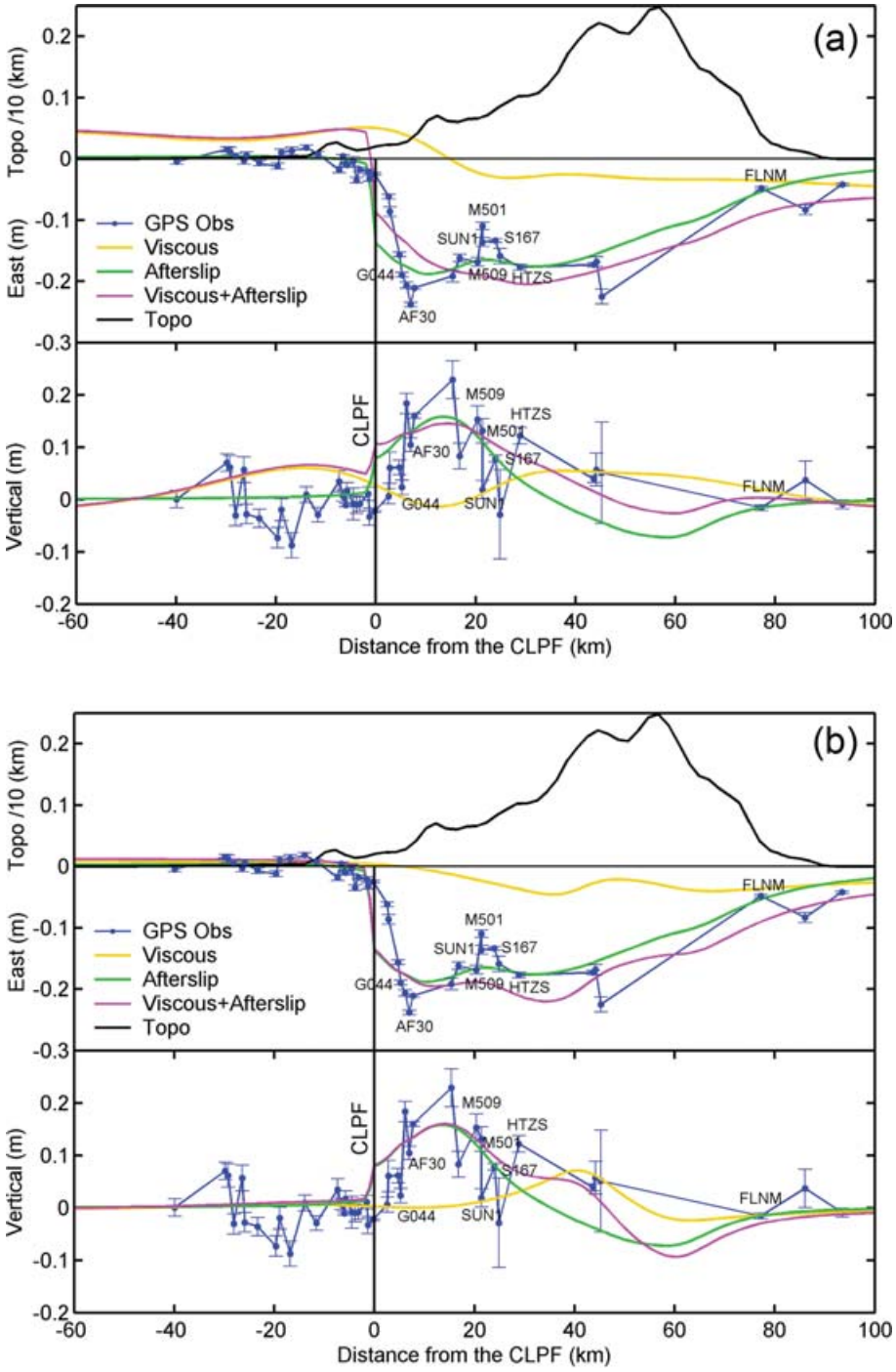

Figure 4. The GPS post-seismic displacements in the 15-month period (blue), predicted viscoelastic displacements in the same period (yellow) and model post-seismic displacements from Yu *et al.* (2003) (green). The GPS displacements are taken from between 23.7° N and 24.0° N and projected onto a profile perpendicular to the fault. The magenta line denotes the combination of viscoelastic displacement and afterslip. The solid black line indicates topography. Results from model at (a) Fig. 3(a) and (b) Fig. 3(b).

to fault slip following an integrated random walk in time. An integrated random walk is slowly varying in time, and may not be optimal for modelling rapid transients immediately following a large event, such as the Chi-Chi earthquake, particularly during the first few observation epochs when the filter estimates are based on few data. The strain rates, however, decay substantially with time, and we have found that the integrated random walk model is more accurate if one takes the data reversed in time. Therefore, we start at the end of the time-series when the strain rates are relatively steady, and work back towards the time of the earthquake. This gives the filter time to adapt to the rapid transients after the earthquake.

We subtract the steady interseismic velocity and offsets due to large aftershocks ($M_w > 6$) from the GPS position time-series. The remaining GPS positions, $X(t)$, can be modelled as

$$X(t) = \int_A S_p(\xi, t - t_0) G^r_{pq}(x, \xi) n_q(\xi)\, dA(\xi) + Ff(t) + L(x, t - t_0) + \varepsilon. \quad (1)$$

The first term represents station movements caused by fault slip, $s_p(\xi, t - t_0)$ at time t and position on the fault ξ. $G^r_{pq}(x, \xi)$ are Green's functions for rectangular fault segments in a layered earth model (Chen *et al.* 1998). In eq. (1), $p, q, r = 1, 2, 3$, summation on repeated indices is implied, and $n_q(\xi)$ is the unit normal to the fault surface $A(\xi)$. The second term $Ff(t)$ accounts for reference frame errors, where F is a Helmert transformation and $f(t)$ is a vector of rigid body translation, rotation and scale factor (Miyazaki *et al.* 2003). The third term is local benchmark motion, which we take to be a Brownian random walk with a $1/f^2$ spectral decay. The last term ε represents observation errors which we assume to be normally distributed with zero mean and covariance $\sigma^2\Sigma^{\mathrm{GPS}}$, where Σ^{GPS} is the covariance matrix of GPS station positions, corrected for secular deformation, and σ^2 is a scale factor that accounts for unmodelled errors in GPS data processing and errors in the secular correction.

The fault geometry is constrained by aftershocks, inversions of coseismic displacement data, and seismic imaging. The Chi-Chi earthquake induced more than 30 000 aftershocks in the 3-month period following the main shock (Fig. 2), with six of them $M_w > 5.8$ (Chi & Dreger 2004). Most aftershocks occurred off the Chelungpu fault (Chang *et al.* 2000; Cheng 2000; Chen *et al.* 2002). The aftershock distribution alone is, therefore, not able to delineate the fault geometry. Seismic reflections lines on the hangingwall of the CLPF provide constraints on the shallow fault structure. Wang *et al.* (2002) show that the CLPF dips to the east 18°–35° with the fault becoming shallower to the north. Levy *et al.* (2005) invert for the coseismic slip distribution using the fault geometry constrained by structural measurements and seismic profiles (Yue *et al.* 2005). However, the fit to the data is actually poorer than the model with a simpler fault geometry (Yu *et al.* 2003).

We use the fault geometry derived by Johnson *et al.* (2001) and Yu *et al.* (2003), based on grid search inversions. The fault geometry is in first-order agreement with previous independent studies. The fault geometry includes a 26° shallow dipping fault connected to a nearly horizontal décollement at a depth of 10 km. The fault length along strike is 90 km and the downdip width of upper and lower segments are 24 and 40 km, respectively. There are 108 fault patches on the entire fault. We did not include the two fault segments at the northern bend of the CLPF in the model of Johnson *et al.* (2001). Earlier analysis by Hsu *et al.* (2002) showed that little post-seismic slip is required on these segments to fit the data; we exclude them here for simplicity.

Previous time-independent inversions revealed substantial afterslip on the décollement well south of the Chi-Chi rupture (Hsu *et al.* 2002; Yu *et al.* 2003). This slip is inferred from accelerated westward displacements at stations CHNL, YUSN and S058, south of the southern end of the rupture (Fig. 1). We consider the possibility that these motions are caused by processes other than localized fault slip on the main shock rupture and décollement, such as triggered afterslip on separate faults well south of the coseismic rupture. Therefore, we conduct inversions both including and excluding these stations. When these stations are included, the fault geometry is extended 20 km to the south along strike.

In the ENIF, we apply spatial smoothing using a finite difference approximation of the Laplacian operator, and non-negativity constraints to ensure the slip-rate distribution is one-sided. Reverse and left-lateral slips are constrained to be positive, consistent with previous analyses of the post-seismic displacement field. The non-negativity of the slip-rate distribution is controlled by a hyperparameter, ρ; a small value of 0.001 m yr^{-1} is used to keep the slip rate from becoming negative (McGuire & Segall 2003).

Other hyperparameters used in the experiment are: τ, which represents the scale factor of benchmark motions, a value of 2 mm yr$^{-0.5}$ is used consistent with previous studies (Langbein & Johnson 1997); σ, which is a scale factor of GPS data covariance. A value of five is suggested for Taiwan GPS network according to previous comparisons on GPS formal errors with baseline repeatability. The hyperparameters for temporal and spatial smoothing of the slip-rate distribution are α and γ, respectively. Ideally, one assigns sufficiently large a priori variances that the final estimates are determined solely by the data. However, the post-seismic GPS displacements contain very short spatial wavelength variations that are difficult to fit with smooth elastic models. Given sufficient flexibility, the ENIF tends to fit every data point, resulting in slip-rate distributions that are extremely variable in the spatial domain. We opt to constrain the filter to yield smoother slip-rate distributions in both space and time. Whether these short wavelength features in the data represent local monument instabilities or other inelastic processes not accounted for in the model is at this point unknown.

We initialize the filter with α of 0.5 ± 4 (actual computations use the log of the parameter to force the hyperparameters to remain positive), and γ of 0.05 ± 2. The spatial smoothing equations scale with the ratio α/γ (McGuire & Segall 2003), so there is a trade-off between spatial and temporal smoothing in the ENIF formulation. Trial and error has shown that by choosing *a priori* variances for α, 0.5 ± 2.0 and, γ, 0.05 ± 1.1, we obtain relatively smooth slip-rate distributions that fit the first-order features in the data. We tested a variety of solutions with differing a priori estimates of the spatial smoothing parameter γ ranging from 0.001 to 0.15. The final values of the ENIF estimates give α ranging from 1.0 to 3.8, with γ ranging from 0.02 to 0.21 (Fig. 5). We use the solution of $\alpha = 1.4$ and $\gamma = 0.053$ for the result presented in this study. This value (indicated by the circle in Fig. 5) gives a reasonable trade-off between minimizing the weighted data residual, without causing the model roughness to become unreasonably large. We emphasize that the slip-rate estimates do not vary significantly for modest changes in either α or γ. In fact, none of our principal conclusions would change by taking the extreme range of solutions indicated in Fig. 5.

5 RESULTS AND DISCUSSION

We first discuss the time-dependent inversion excluding three southern stations, CHNL, YUSN and S058. The ENIF successfully predicts the temporal evolution of the post-seismic displacements, as shown by the fit of the model predictions to the GPS time-series for selected continuous and campaign GPS sites (Fig. 6). Our preferred model results in a weighted rms of 0.003 m, although the fit of the vertical component is less satisfactory due to spatially localized signals in the GPS observations that are difficult to fit with a smooth elastic model (Fig. 7).

The cumulative displacements in the 15-month period following the earthquake show significant afterslip of about 0.4 and 0.3 m near the epicentre and downdip of coseismic rupture, respectively (Fig. 7). Maximum slip of 0.57 m occurs to the east of the epicentre, an area of high aftershock activity (Figs 2a and 7a). The time-dependent inversion including three southern stations, CHNL, YUSN and S058, adds substantial slip on the southern CLPF as shown in Fig. 8, while slip on the remainder of the fault is essentially unchanged (compare to Fig. 7). To the south of the coseismic rupture, we find a NW–SE trending zone of aftershocks (120.9°E, 23.4°N) separating regions with large and small afterslip to the east

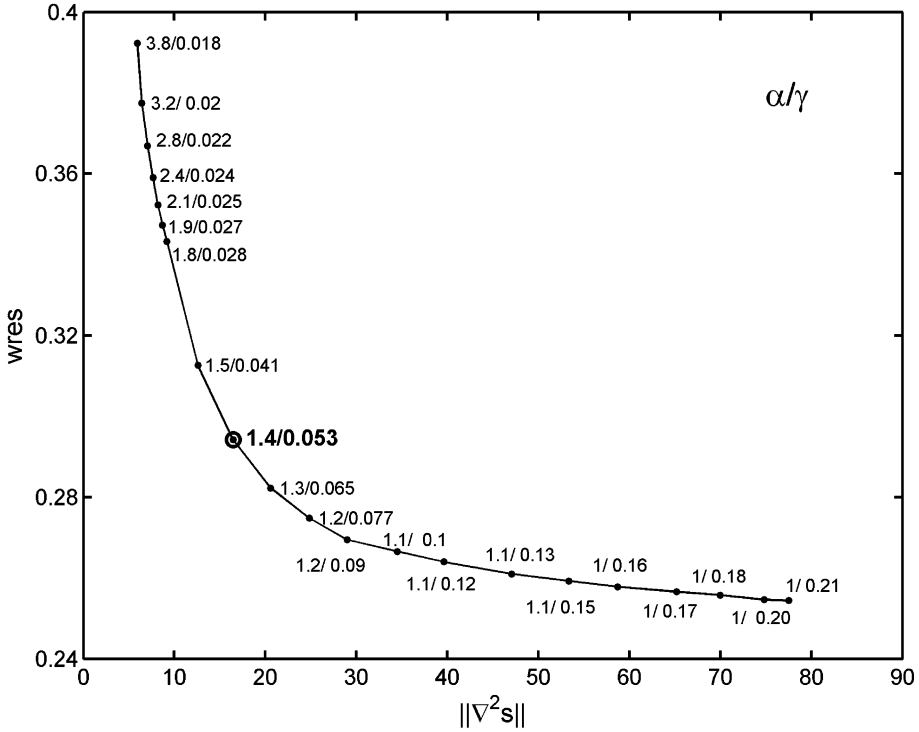

Figure 5. The trade-off between weighted rms residual and model roughness. The values denote two hyperparameters α and γ, respectively. The optimal values are in bold.

and west, respectively. Some portion of the post-seismic displacement near YUSN may be associated with afterslip of the M_w 6.2 aftershock immediately following the main shock. Because we cannot be certain of the origin of the post-seismic deformation near these southern stations, we focus on results without the southern three sites in the following discussion.

We find the highest slip rates of about 1–1.5 m yr^{-1} immediately after the earthquake occur near the hypocentral region and on the deeper décollement (Fig. 9). The highest slip rates and cumulative slip surround the region of greatest coseismic slip, which was located north of the hypocentre on the shallow thrust ramp (Figs 7a and 10). Over the 15-month period, the spatial distribution of slip rate remains roughly stationary, while the magnitude of the slip rates decay with time. However, the shallow slip rates decay more rapidly than the deep slip rates (Figs 9 and 10). The slip rate on the décollement after 15 months is still twice the interseismic creep rate (0.04 m yr^{-1}) (Dominguez *et al.* 2003; Hsu *et al.* 2003).

To quantify the variation in slip rate with time, we divided the fault zone into three regions (Fig. 9): the northern CLPF (N-CLPF, A) where the maximum coseismic slip occurred, the southern CLPF (S-CLPF, B), and the lower décollement (C). The average slip rates in these regions are shown in Fig. 11(a). These plots indicate that afterslip evolution on the northern CLPF, where maximum coseismic slip occurred, is quite different from that on the southern CLPF and the lower décollement. Bearing in mind that post-seismic slip on the northern CLPF is small and may not be reliable, the average slip rate there increased for the first 2 months but then decreased to a value of less than 0.1 m yr^{-1}. Afterslip on the southern CLPF started at a higher rate of about 1.4 m yr^{-1} and decayed more rapidly than that on the lower décollement, consistent with the distribution of cumulative fault slip in Fig. 10. The cumulative averaged slips over 15 months on the northern CLPF, the southern CLPF, and the lower décollement are 0.09, 0.29 and 0.30 m, respectively.

Yu *et al.* (2003) use an elastic half-space model with shear modulus of 30 GPa and find afterslip over the first 15 months following the main shock has a geodetic moment of 4.7×10^{19} N m, with 80 per cent of which is on the décollement. Our time-dependent inversion using a layered earth model shows slightly less accumulated geodetic moment, 3.8×10^{19} N m (13 per cent of the coseismic moment), over the same period, while the ratio of moment release on the décollement to the total moment is similar to that found by Yu *et al.* (2003). This is in marked contrast to slip in the earthquake, which occurred dominantly on the shallow thrust ramp. Johnson & Segall (2004) found that only 20 per cent of the coseismic moment release took place on the décollement. We emphasize these features persist no matter which combination of smoothing parameters is chosen in Fig. 5. For inversions including the three southern stations, the geodetic moment is 5.4×10^{19} N m (Fig. 8), which is larger than all previous results and suggests significant post-seismic deformation south of the rupture area.

An important and consistent result of all the afterslip inversions is that post-seismic slip surrounds the region of greatest coseismic slip during the Chi-Chi earthquake (Figs 7 and 8). The time-dependent inversions presented here show that the temporal variation of slip rate is different on the northern and southern CLPF (Fig. 11a). This may be taken to indicate that either the material properties or the stress state vary along the strike of the fault, such that the southern CLPF experienced less coseismic deformation, but larger post-seismic slip than that on the northern CLPF. In terms of spatially variable friction properties, one possibility is that the regions of substantial afterslip are steady-state velocity strengthening, and are driven into accelerated creep due to the coseismic stress change. However, earthquake nucleation requires velocity-weakening friction (Ruina 1983). Thus, the presence of substantial afterslip near the hypocentre argues against velocity strengthening in this region, where the earthquake initiated. An alternative possibility is that

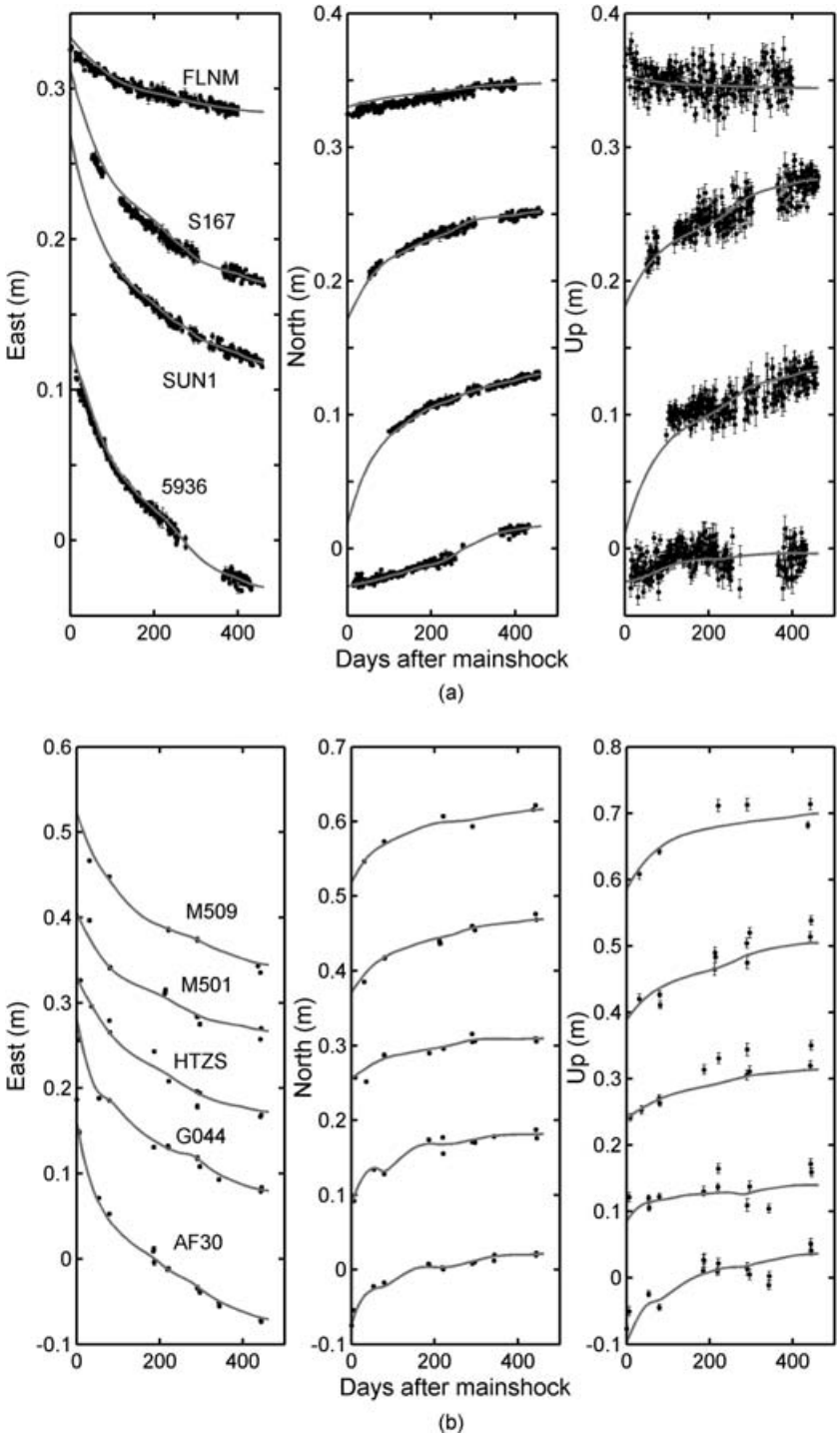

Figure 6. Comparisons between observed GPS displacements and that predicted by the ENIF. Time-series of east, north and vertical components are denoted by black dots with one sigma error bars. Solid lines indicate predicted displacements from the ENIF. (a) Selected continuous stations and (b) selected campaign stations.

these regions exhibit potentially unstable friction (velocity weakening) but that for dynamic reasons (presumably low initial stress state) slipped aseismically following the main shock. This scenario requires substantial afterslip in a region that slipped coseismically, a feature that has not been observed in simulations with rate-state friction to date. Determining which of these scenarios, or others, is correct would have important implications for understanding fault dynamics as well as future seismic hazards.

The seismic moment released by aftershocks during the 15 month time period for which we have GPS data is 6.6×10^{18} N m, about 17 per cent of the post-seismic geodetic moment. However, the seismic moment, 85 per cent of which was released before the end of 1999 (Kao *et al.* 2002), decays much faster than the geodetic moment. We show the temporal evolution of cumulative post-seismic displacement and cumulative number of aftershocks in Figs 11(b) and (c), which illustrates that the rate of aftershocks decays faster

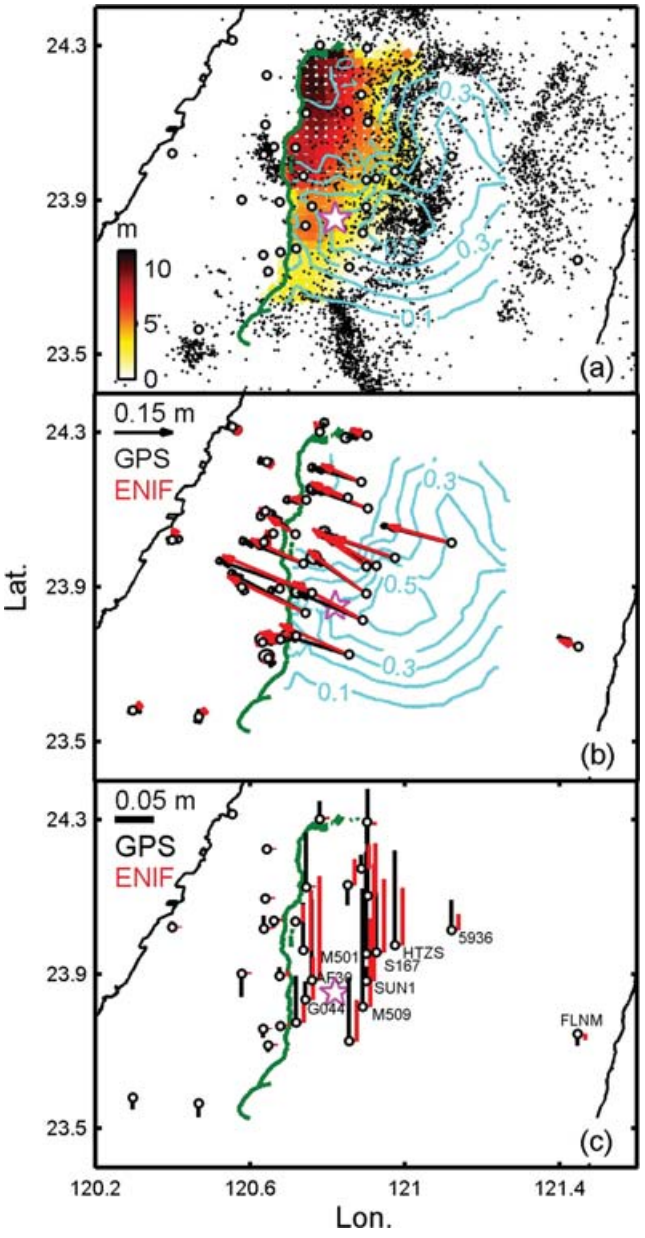

Figure 7. (a) Coseismic and post-seismic slip distributions projected on the surface. Coseismic slip is shown in colour (Levy *et al.* 2005). Post-seismic slip indicated by blue contours at 0.1 m interval. White circles indicate locations of GPS stations. The black dots are aftershocks during the same period. The pink star indicates the epicentre of the Chi-Chi main shock. (b) Cumulative GPS displacements in the 15-month period following the Chi-Chi earthquake (Yu *et al.* 2003) versus predictions from the ENIF. Horizontal displacements from GPS and ENIF are shown by black and red vectors, respectively. Error ellipses are 95 per cent confidence. (c) Vertical displacements (black) and predictions from ENIF (red).

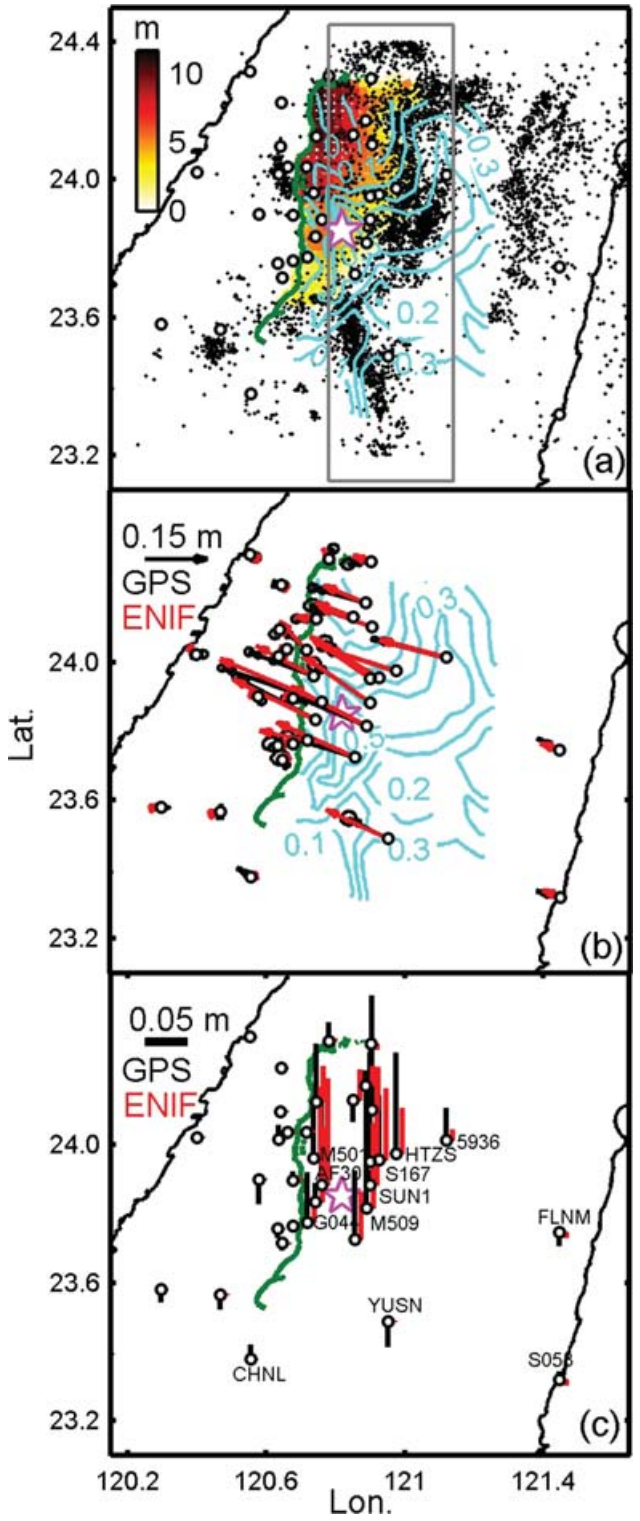

Figure 8. Similar to Fig. 7 but the slip distribution obtained by including stations CHNL, YUSN and S058 on the eastern and southern CLPF. Grey box at (a) indicates the region chosen to count aftershocks in Perfettini & Avouac (2004).

than the afterslip. This statement is also true when we compare the aftershocks and the afterslip in the same region as used by Perfettini & Avouac (2004, Fig. 5) to count aftershocks. Even though the first GPS displacement is obtained 4 days after the main shock, such that the first few days of post-seismic deformation is underestimated, this does not influence the comparison of afterslip and aftershocks, as the aftershocks span the same time interval. Because the largest aftershocks occurred early in the sequence, the moment-rate decays even more rapidly than the seismicity-rate.

The data imply that the bulk of the afterslip is aseismic and that the aftershock rate is not proportional to the post-seismic slip rate as suggested by Perfettini & Avouac (2004). These authors used the displacements at a single station, I007, as a proxy for afterslip.

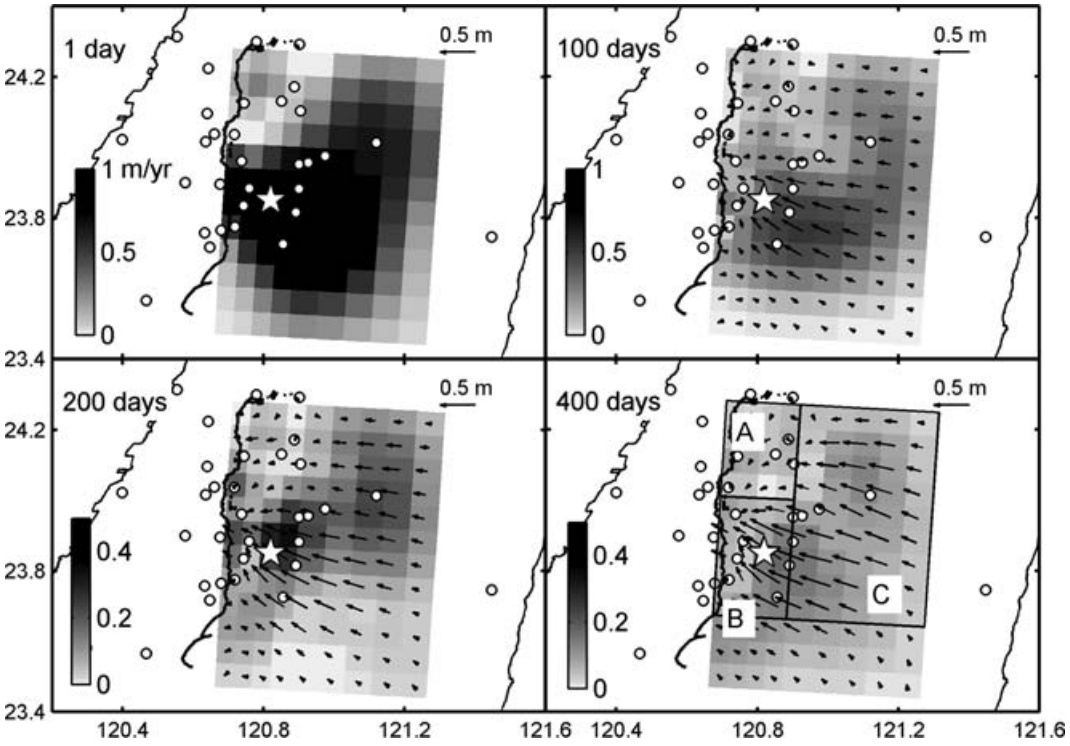

Figure 9. Snapshots of the spatiotemporal slip-rate distributions inverted from post-seismic GPS data with the time indicated in the top left corner. The grey scale indicates the magnitude of slip rate. The black vectors denote the cumulative slip. The star denotes the epicentre of the Chi-Chi main shock. White circles indicate locations of GPS sites. Black boxes in bottom right panel indicate the regions used in Fig. 11.

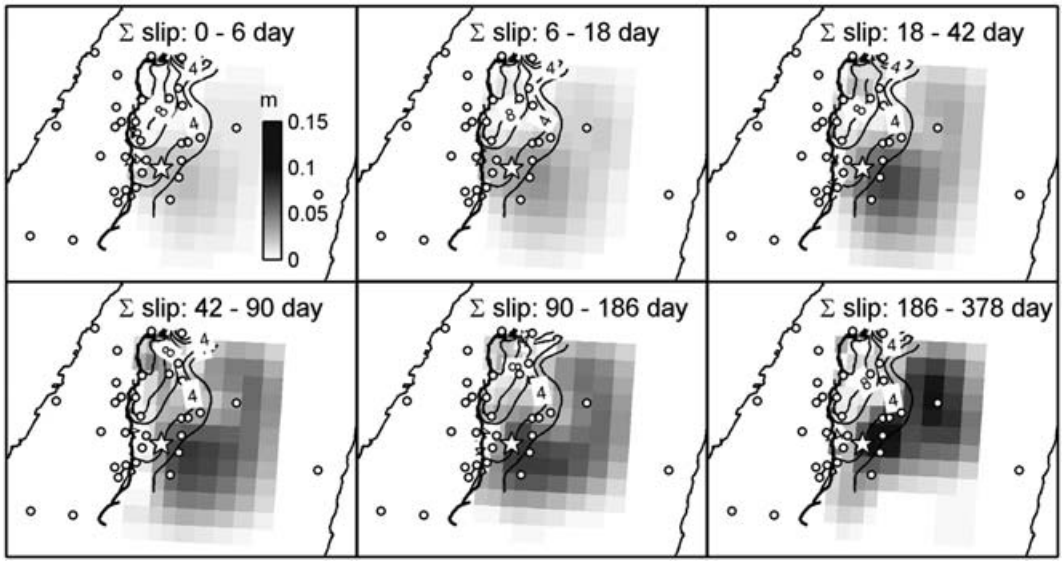

Figure 10. Integrated post-seismic slip over consecutive periods of 6, 12, 24, 48, 96 and 192 days after the Chi-Chi main shock. The grey scale is cumulative slip for the period specified in the top corner. Black contours show the distribution of coseismic slip at 2 m interval (Levy *et al.* 2005). The white star denotes the epicentre. White circles indicate locations of GPS sites.

Station I007 is located south of the epicentre in a region strongly influenced by shallow slip. More importantly, the monument was disturbed by the M_w 6.3 1999 September 25 aftershock; indeed the post-seismic displacement of I007 is anomalous when compared to most other nearby stations. We conclude that the displacements at this particular station do not provide a representative measure of afterslip, particularly downdip of the main shock rupture.

Despite the fact that many large aftershocks were located to the east of the epicentre, where maximum afterslip occurred, the spatial distribution of aftershocks and afterslip are also noticeably different (Fig. 7). There are two prominent north–south trending bands of aftershocks. The westerly band trends north from the area of maximum afterslip (latitude 23.8°), paralleling the western edge of the afterslip zone from latitude 24.0° to 24.2°. In contrast, the afterslip distribution has a backwards L shape with substantial slip at shallow

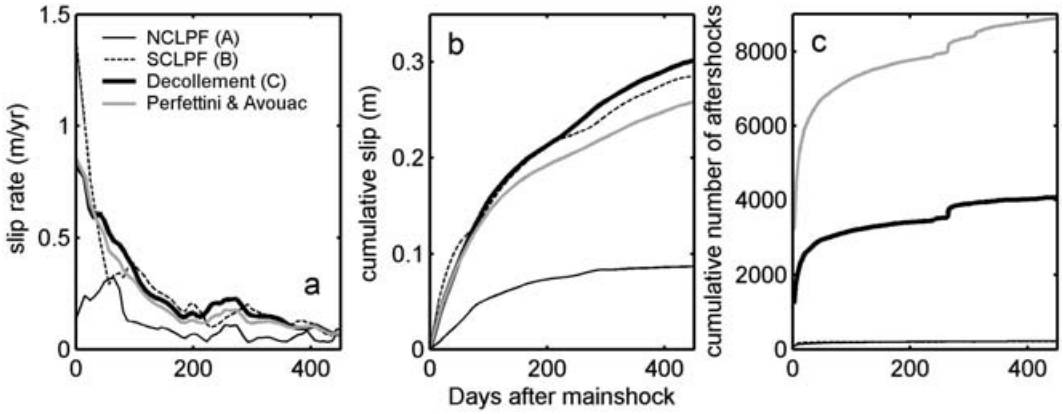

Figure 11. Temporal evolution of (a) Slip rate, (b) Cumulative slip, and (c) Cumulative number of aftershocks, for there selected areas (A–C) are indicated in Fig. 9. The slip-rate and cumulative slip curves labelled 'Perfettini and Avouac' refer to slip averaged over the box used by Perfettini & Avouac (2004) to count aftershocks, also shown in Fig. 8(a) here.

depths near the epicentre (Fig. 7a). Most aftershocks on the northern CLPF (near 121°E, 24.1°N) occur at the downdip edge of the coseismic rupture, but updip of where afterslip was concentrated. Seismicity before the Chi-Chi earthquake occurred in a similar location, suggesting creep on the décollement (Dominguez *et al.* 2003). A prominent band of aftershocks trending NNW–SSE south of the main shock epicentre (23.4°N to 23.6°N) possibly is associated with a large strike-slip aftershock (Chi & Dreger 2004). A second parallel band of seismicity, offset to the east, is located near the downdip limit of afterslip. It should be kept in mind that the focal depths of the aftershocks (Fig. 2b) are widely distributed from near the surface to as much as 30 km near the Chi-Chi rupture, while the maximum afterslip inferred from the geodetic observations occurred at a depth of 10 km. In summary then, the spatial association of aftershocks and post-seismic slip is complex. There are areas with substantial slip and seismicity, but others exhibit large afterslip with no earthquakes, while in other areas aftershocks seem to follow the updip edge of the inferred afterslip.

Perfettini & Avouac (2004) fit both the aftershock sequence and afterslip, inferred from a single continuous GPS station, and concluded they follow the same temporal evolution. However, when examined in greater detail we find that the aseismic slip and aftershocks have complex spatial distributions and that the aftershock rate decays more rapidly than the afterslip rate. Furthermore, Perfettini & Avouac (2004) assume that the post-seismic deformation occurs below the coseismic slip area where the stress increased after the main shock, which is not consistent with inversions that find significant afterslip on the southern portion of the shallow ramp fault (Fig. 7). Further investigation will be required to clarify the role of post-seismic processes in controlling the occurrence of aftershocks.

6 CONCLUSIONS

Post-seismic GPS displacements over a 15-month period starting 4 days after the Chi-Chi earthquake are better explained by afterslip than viscoelastic relaxation. The optimal afterslip model shows the highest slip rates surrounding the region of greatest coseismic slip with the maximum post-seismic slip of 0.57 m east of the hypocentral region. The total accumulated geodetic moment is 3.8×10^{19} N m, 80 per cent of that is on the décollement. In contrast to that only 20 per cent of the coseismic geodetic moment was released on the décollement. The deep post-seismic slip on the décollement is consistent with models involving velocity-strengthening friction below the rupture zone. However, afterslip detected at seismogenic depths on the southern end of the rupture is more difficult to understand. Further elucidation of the frictional properties that would give rise to the observed afterslip at seismogenic depths would have important implications for our understanding of fault dynamics as well as future earthquake hazards on the Chelungpu fault. We find that the aftershock rate decayed more rapidly than the rate of afterslip and the two spatial distributions are only somewhat correlated. These observations suggest that aftershocks may not be completely controlled by afterslip as has been suggested.

ACKNOWLEDGMENTS

We are grateful to many colleagues at the Institute of Earth Sciences, Academia Sinica and the Land Survey Bureau, Ministry of Interior who have participated in collecting GPS data. We thank Mark Simons and Jean-Philippe Avouac for permission to use FEM modelling results obtained by Y.J. Hsu at Caltech as part of a research project funded by EAR-0537625. We are grateful for constructive comments from Dr John Beavan and two anonymous reviewers, as well as to Shinichi Miyazaki, Jessica Murray, and Eric A. Hetland. This study was supported by the Institute of Earth Sciences, Academia Sinica, the National Science Council of the Republic of China grant NSC 94-2119-M001-008, the National Science Foundation grant EAR-0106695 to Stanford University, the National Science Foundation grant EAR-0537625 to Caltech and the Gordon and Betty Moore Foundation. This is a contribution of the Institute of Earth Sciences, Academia Sinica, IESAS1143, Caltech Seismological Laboratory contribution number 9161 and Caltech Tectonics Observatory contribution number 58.

REFERENCES

Burgmann, R., Ergintav, S., Segall, P., Hearn, E.H., McClusky, S., Reilinger, R.E., Woith, H. & Zschau, J., 2002. Time-dependent distributed afterslip on and deep below the Izmit earthquake rupture, *Bull. seism. Soc. Am.,* **92,** 126–137.

Chang, C.H., Wu, Y.M., Shin, T.C. & Wang, C.Y., 2000. Relocation of the 1999 Chi-Chi earthquake in Taiwan, *TAO,* **11,** 581–590.

Chen, C.H., Teng, T.L. & Gung, Y.C., 1998. Ten-second Love-wave propagation and strong ground motions in Taiwan, *J. Geophys. Res.,* **103,** 21253–21273.

Chen, K.C., Huang, B.S., Wang, J.H. & Yen, H.Y., 2002. Conjugate thrust faulting associated with the 1999 Chi-Chi, Taiwan, earthquake sequence, *Geophys. Res. Lett.,* **29,** doi:10.1029/2001GL014250.

Cheng, W.B., 2000, Three-dimensional crustal structure around the source area of the 1999 Chi-Chi earthquake in Taiwan and its relation to the aftershock locations, *TAO,* **11,** 643–660.

Chi, W.C. & Dreger, D., 2004, Crustal deformation in Taiwan: Results from finite source inversions of six $M_w > 5.8$ Chi-Chi aftershocks, *J. Geophys. Res.,* **109,** doi:10.1029/2003JB002606.

Dominguez, S., Avouac, J.P. & Michel, R., 2003. Horizontal coseismic deformation of the 1999 Chi-Chi earthquake measured from SPOT satellite images: Implications for the seismic cycle along the western foothills of central Taiwan, *J. geophys. Res.,* **108,** doi:10.1029/2001JB000951.

Fialko, Y., 2004. Evidence of fluid-filled upper crust from observations of postseismic deformation due to the 1992 M(w)7.3 Landers earthquake, *J. geophys. Res.,* **109,** doi:10.1029/2004JB002985.

Hsu, Y.J., Bechor, N., Segall, P., Yu, S.B., Kuo, L.C. & Ma, K.F., 2002. Rapid afterslip following the 1999 Chi-Chi, Taiwan earthquake, *Geophys. Res. Lett.,* **29,** doi:10.1029/2002GL014967.

Hsu, Y.J., Simons, M., Yu, S.B., Kuo, L.C. & Chen, H.Y., 2003. A two-dimensional dislocation model for interseismic deformation of the Taiwan mountain belt, *Earth planet. Sci. Lett.,* **211,** 287–294.

Hugentobler, U., Schaer, S. & Fridez P., 2001. Bernese GPS software v. 4.2, Astronomical Institute, University of Berne, Switzerland, 515pp.

Ji, C., Helmberger, D.V., Song, T.R.A., Ma, K.F. & Wald, D.J., 2001. Slip distribution and tectonic implication of the 1999 Chi-Chi, Taiwan, Earthquake, *Geophys. Res. Lett.,* **28,** 4379–4382.

Johnson, K.M. & Segall, P., 2004. Imaging the ramp-decollement geometry of the Chelungpu fault using coseismic GPS displacements from the 1999 Chi-Chi, Taiwan earthquake, *Tectonophysics,* **378,** 123–139.

Johnson, K.M., Hsu, Y.J., Segall, P. & Yu, S.B., 2001. Fault geometry and slip distribution of the 1999 Chi-Chi, Taiwan earthquake imaged from inversion of GPS data, *Geophys. Res. Lett.,* **28,** 2285–2288.

Jonsson, S., Segall, P., Pederson, R. & Bjornsson, G., 2003. Post-earthquake ground movements correlated to pore-pressure transients, *Nature,* **424,** 179–183.

Kao, H., Liu, Y.H., Liang, W.T. & Chen, W.P., 2002. Source parameters of regional earthquakes in Taiwan: 1999-2000 including the Chi-Chi earthquake sequence, *TAO,* **13,** 279–298.

Langbein, J. & Johnson, H., 1997. Correlated errors in geodetic time series: Implications for time-dependent deformation, *J. geophys. Res.,* **102,** 591–603.

Lee, J.C., Chu, H.T., Angelier, J., Chan, Y.C., Hu, J.C., Lu, C.Y. & Rau, R.J., 2002. Geometry and structure of northern surface ruptures of the 1999 Mw = 7.6 Chi-Chi Taiwan earthquake: influence from inherited fold belt structures, *J. Struct. Geol.,* **24,** 173–192.

Levy, F., Hsu, Y.J., Simons, M., Leprince, S. & Avouac, J.P., 2005. Distribution of coseismic slip for the 1999 ChiChi Taiwan earthquake: New data and implications of varying 3D fault geometry, AGU Fall Meeting Suppl., Abstract T41B-1305.

Lin, C.H., 2000. Thermal modeling of continental subduction and exhumation constrained by heat flow and seismicity in Taiwan, *Tectonophysics,* **324,** 189–201.

Loevenbruck, A., Cattin, R., Pichon, X. Le, Dominguez, S. & Michel, R., 2004. Coseismic slip resolution and post-seismic relaxation time of the 1999 Chi-Chi, Taiwan, earthquake as constrained by geological observations, geodetic measurements and seismicity, *Geophys. J. Int.,* **158,** 310–326.

Ma, K.F., Mori, J., Lee, S.J. & Yu, S.B., 2001. Spatial and temporal distribution of slip for the 1999 Chi-Chi, Taiwan, earthquake, *Bull. seism. Soc. Am.,* **91,** 1069–1087.

Ma, K.F., Chan, C.H. & Stein, R.S., 2005. Response of seismicity to Coulomb stress triggers and shadows of the 1999 M-w = 7.6 Chi-Chi, Taiwan, earthquake, *J. geophys. Res.,* **110,** doi:10.1029/2004JB003389.

McGuire, J.J. & Segall, P., 2003. Imaging of aseismic fault slip transients recorded by dense geodetic networks, *Geophys. J. Int.,* **155,** 778–788.

Melosh, H.J. & Raefsky, A., 1980. The dynamical origin of subduction zone topography, *Geophys. J. R. astr. Soc.,* **60,** 333–354.

Miyazaki, S., McGuire, J.J. & Segall, P., 2003. A transient subduction zone slip episode in southwest Japan observed by the nationwide GPS array, *J. geophys. Res.,* **108,** doi:10.1029/2001JB000456.

Miyazaki, S., Segall, P., Fukuda, J. & Kato, T., 2004. Space time distribution of afterslip following the 2003 Tokachi-oki earthquake: Implications for variations in fault zone frictional properties, *Geophys. Res. Lett.,* **31,** doi:10.1029/2003GL019410.

Miyazaki, S., Segall, P., McGuire, J.J., Kato, T. & Hatanaka, Y., 2006. Spatial and temporal evolution of stress and slip rate during the 2000 Tokai slow earthquake, *J. geophys. Res.,* **111,** doi:10.1029/2004JB003426.

Nur, A. & Mavko, G., 1974. Postseismic viscoelastic rebound, *Science,* **183,** 204–206.

Perfettini, H. & Avouac, J.P., 2004. Postseismic relaxation driven by brittle creep: A possible mechanism to reconcile geodetic measurements and the decay rate of aftershocks, application to the Chi-Chi earthquake, Taiwan, *J. geophys. Res.,* **109,** doi:10.1029/2003JB002488.

Pollitz, F.F., 2001. Viscoelastic shear zone model of a strike-slip earthquake cycle, *J. geophys. Res.,* **106,** 26541–26560.

Rau, R.J. & Wu, F.T., 1995. Tomographic imaging of lithospheric structures under Taiwan, *Earth planet. Sci. Lett.,* **133,** 517–532.

Ruina, A., 1983. Slip instability and state variable friction laws, *J. geophys. Res.,* **88,** 359–370.

Segall, P., Burgmann, R. & Matthews, M., 2000. Time-dependent triggered afterslip following the 1989 Loma Prieta earthquake, *J. geophys. Res.,* **105,** 5615–5634.

Segall, P. & Matthews, M., 1997. Time dependent inversion of geodetic data, *J. geophys. Res.,* **102,** 22391–22409.

Sheu, S.Y. & Shieh, C.F., 2004. Viscoelastic-afterslip concurrence: a possible mechanism in the early post-seismic deformation of the M-w 7.6, 1999 Chi-Chi (Taiwan) earthquake, *Geophys. J. Int.,* **159,** 1112–1124.

Wang, C.Y., Li, C.L. & Yen, H.Y., 2002. Mapping the northern portion of the Chelungpu fault, Taiwan by shallow reflection seismics, *Geophys. Res. Lett.,* **29,** doi:10.1029/2001GL014496.

Williams, C.A. & Richardson, R.M., 1991. A rheologically layered 3-Dimensional model of the San-Andreas Fault in central and southern California, *J. geophys. Res.,* **96,** 16 597–16 623.

Yu, S.B. *et al.*, 2001. Preseismic deformation and coseismic displacements associated with the 1999 Chi-Chi, Taiwan, earthquake, *Bull. seism. Soc. Am.,* **91,** 995–1012.

Yu, S.B., Hsu, Y.J., Kuo, L.C., Chen, H.Y. & Liu, C.C., 2003. GPS measurement of postseismic deformation following the 1999 Chi-Chi, Taiwan, earthquake, *J. geophys. Res.,* **108,** doi:10.1029/2003JB002396.

Yue, L.F., Suppe, J. & Hung, J.H., 2005. Structural geology of a classic thrust belt earthquake: the 1999 Chi-Chi earthquake Taiwan ($M_w = 7.6$), *J. Struct. Geol.,* **27,** 2058–2083.

Zeng, Y.H. & Chen, C.H., 2001. Fault rupture process of the 20 September 1999 Chi-Chi, Taiwan, earthquake, *Bull. seism. Soc. Am.,* **91,** 1088–1098.